Minimum-Cost Path Framework for 3D Airway Centerline Extraction

Malte Silbernagel[1][0009−0008−5606−0762], Jens Petersen[1,2][0000−0003−0138−0693], and Marleen de Bruijne[1,3][0000−0002−6328−902X]

[1] Department of Computer Science, University of Copenhagen, Copenhagen, Denmark
[2] Department of Oncology, Rigshospitalet, Copenhagen, Denmark
[3] Department of Radiology and Nuclear Medicine, Erasmus MC - University Medical Center Rotterdam, The Netherlands

Abstract. Accurate extraction of curve skeletons provides a compact one-dimensional representation of complex three-dimensional structures and plays a fundamental role in numerous medical image analysis and machine intelligence applications. Despite its importance, robust centerline extraction from volumetric medical images remains challenging, particularly in the presence of segmentation artifacts, small vessels, and complex vascular topology. In this work, we propose a fully automated framework for centerline detection of complex branching airway trees from 3D segmentation masks. Starting from a root node in the trachea, the method propagates two wavefronts with distinct cost functions: the first is used to identify terminal endpoints, while the second is used to trace the centerline paths back towards the root by following the medial structure of the airway tree. The proposed approach accurately recovers full airway topology, including branching points and tree hierarchy at arbitrary depth, and provides a robust out-of-the-box implementation applicable to any arbitrary 3D airway segmentation without additional adaptation. The source code is publicly available at https://github.com/maltesilber/AirwayParser.

Keywords: Airway Morphology · Skeletonization · Minimum-Cost Path

1 Introduction

Three-dimensional centerline extraction is a fundamental step in the analysis of tree-like structures [3,10,19]. In biomedical imaging, the accuracy of the extracted centerline directly propagates to downstream analyses. In airway analyses the computation of morphological biomarkers [5,11] and segmentation quality metrics are generally derived from the centerline [9,23]. Deviations from the true medial axis can compound through analysis pipelines, leading to unreliable quantitative outcomes.

We noticed a gap between methodological advances in skeletonization algorithms [18] and the availability of robust, ready-to-use software implementations. Especially with the rise of deep learning in medical imaging [15] and the

dominance of Python-based ecosystems in modern pipelines. Off-the-shelf implementations [20,8] are error-prone for airways. They suffer from spurious branches under boundary noise, loops inherited from mask handles, and anisotropy-blind operation on the voxel lattice. Other more advanced general-purpose methods [6] also stop at the medial axis and leave the parsing into a structured tree, branch point detection, generation assignment to the user. Researchers therefore either rely on ad hoc post-processing rules, re-implement published methods, or build custom solutions [24], creating barriers to adoption, limiting reproducibility, and hindering fair comparison across studies.

To address these gaps, we propose a robust airway tree parsing framework at sub-voxel resolution. From a root node in the trachea, we propagate two wavefronts with distinct cost functions. The first identifies the terminal endpoints as the most distal points of the tree, while the second traces each endpoint back to the root along its medial axis (Fig. 1). The branch hierarchy emerges from the paths that trace to the same root node. This enables an intuitive recovery of the airway topology. The method is provided as a ready-to-use Python implementation, allowing straightforward integration into modern imaging and deep learning workflows.

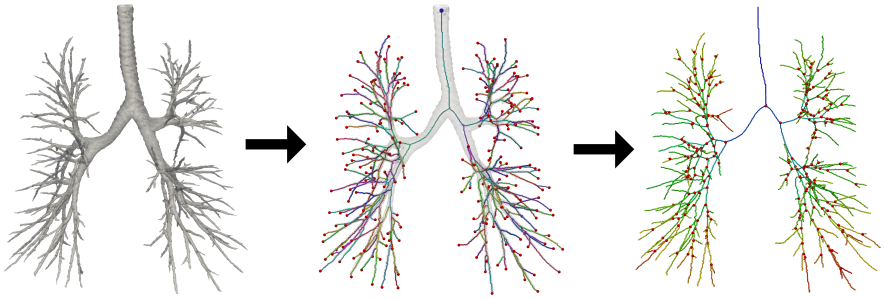

Fig. 1. High-level overview of the proposed method. Given a 3D airway segmentation, we first extract all centerline paths by tracing back from every endpoint to the root node. These paths are then parsed into a curve skeleton from which branching points and tree hierarchy are extracted.

2 Related Work

The predominant approach to curve-skeleton extraction is iterative thinning due to its simplicity and availability in ready-to-use software [8,20]. While preserving connectivity, these methods are sensitive to boundary noise and operate on the voxel grid. Airway pipelines [12,2,14] built on thinning [13] and address limitations in post-processing. Sub-voxel accuracy is recovered only afterwards by re-centering and spline fitting, and spurious branches and loops resulting from boundary noise are stripped by dedicated passes such as graph-search loop

removal and breadth-first pruning. The branch hierarchy is read off from each skeleton voxel's neighborhood connectivity, where a single spur or one-voxel gap misroutes the parse. With implementations distributed in MATLAB, outside the Python and deep-learning ecosystems now standard in medical imaging. In [24] a simple Python tool parses a thinned segmentation into branches by deleting skeleton voxels with more than three skeleton neighbors, cutting the skeleton at every fork, and iteratively merges the branches that violate the expected tree topology. AirMorph [22] replaces the thinning with the parameter-dependent path-cost skeletonization of TEASAR [16] but retains the same tree parser.

Minimum-cost-path methods [7,6] instead evolve a front through the segmented object, guided by a medial function, and trace minimum-cost paths through the arrival-time field, resulting in a global, topology-aware formulation well-suited to tubular structures such as airways. Its accuracy hinges on the medial function, e.g., distance-transform formulations [4,7] are conceptually simple and efficient but degenerate to medial sheets in 3D. Hence, paths from different branches can run in parallel rather than converging at the true bifurcation, delaying branch detection and corrupting downstream airway measurements.

In [6] this is addressed by a medial axis that is chosen based on the magnitude of Gradient Vector Flow (GVF) [21]. Here the GVF serves as a vector field that smoothly propagates local boundary information into the interior and forms a flow towards one medial curve insensitive to boundary noise. We use the divergence of the GVF [21] inside the airway mask. Regions where airway branches merge exhibit a convergence of the inward-directed flow from several directions. Consequently, these junctions generate strong negative sinks in the vector field. This property makes the formulation particularly suitable for airway analysis as it encourages the shortest paths to merge as soon as possible and therefore preserves the branching topology.

3 Methods

Given an airway segmentation mask with the domain $\Omega \subset \mathbb{R}^3$, we aim to retrieve a skeleton that encodes its topology. Airways extend outwards from a root node $\mathbf{x}_r \in \mathbb{R}$, the common proximal origin of the airway tree, into one of the $i = 1, ..., n$ endpoint nodes $\mathbf{e}_i$ of n different terminal branches of the structure. Its medial axis constructs a graph G that connects each endpoint with the common source. Therefore, the problem of constructing G can be reformulated as the task of finding the individual medial axis between each pair of nodes $\{(\mathbf{x}_r, \mathbf{e}_i)\}_{i=1}^{n}$. The union of all curves forms a tree graph corresponding to the centerline of the entire structure. This simplifies the problem down to locating the root node, each endpoint and then computing the medial axis between each pair.

3.1 Shortest Path Finding

The medial axis between two points can be computed as a minimum-cost path through the domain [7], where the cost function enforces the *centeredness* of the path by favoring locations close to the object center.

Let $\mathbf{x}_0 \in \mathbb{R}^n$ be a source point and $\mathbf{x}$ be an arbitrary point in the domain. A path γ from $\mathbf{x}_0$ to $\mathbf{x}$ is a continuous curve $\gamma : [0, L] \to \mathbb{R}^n$ with $\gamma(0) = \mathbf{x}_0$ and $\gamma(L) = \mathbf{x}$, where L is the arc length of the path.

The minimum-cost function $T(\mathbf{x})$ is defined as the minimum cumulative travel cost over all possible paths connecting $\mathbf{x}_0$ to $\mathbf{x}$

$$T(\mathbf{x}) = \min_{\gamma:\mathbf{x}_0\to\mathbf{x}} \int_0^L U(\gamma(s))\, ds \tag{1}$$

where $U : \mathbb{R}^n \to \mathbb{R}^+$ is a cost function that assigns a cost density to each point in the domain, and ds is the arc length element along the path. The solution $T(\mathbf{x})$ satisfies the eikonal equation with a speed function F,

$$|\nabla T(\mathbf{x})|\, F(\mathbf{x}) = 1, \qquad F(\mathbf{x}) = 1/U(\mathbf{x}). \tag{2}$$

where the speed function is the reciprocal of the cost U.

The Fast Marching Method (FMM) [1] provides an efficient approximation of (1) by solving the corresponding Eikonal formulation Equation (2). Lastly, to extract centerlines, we design the cost function to penalize paths near object boundaries and favor paths through the center:

$$U(\mathbf{x}) = \exp(-\alpha m(\mathbf{x})), \tag{3}$$

where $m(\mathbf{x})$ is a medial function with high values in the center and $\alpha \geq 0$ controls the attraction strength towards the centerline.

Root and Endpoint Detection: The quality of the extracted centerline strongly depends on the choice of the medial function. We formulate a medial function based on the divergence of the GVF [21]. The GVF provides a globally smooth vector field that propagates local edge information into regions where the image gradient is weak or absent.

Let $f : \mathbb{R}^3 \to \mathbb{R}$ be a scalar image function and let the GVF field be represented as the vector field $V(x) = [u(\mathbf{x}), v(\mathbf{x}), w(\mathbf{x})]^T$. The GVF is defined as the minimum of the energy functional:

$$\begin{aligned} E(\mathbf{V}) = \iiint \mu \left(|\nabla u(\mathbf{x})|^2 + |\nabla v(\mathbf{x})|^2 + |\nabla w(\mathbf{x})|^2\right) \\ + |\nabla f(\mathbf{x})|^2 |\mathbf{V}(\mathbf{x}) - \nabla f(\mathbf{x})|^2 \, d\mathbf{x}, \end{aligned} \tag{4}$$

where $\mu > 0$ controls the smoothness and $f(\mathbf{x})$ is an edge map. The first term encourages smoothness of the vector field, whereas the second term forces the field to remain close to the image gradient in regions with strong image variation. For our purposes we choose $f(\mathbf{x}) = \mathbf{1}_{\mathbf{x}\in\Omega}$ where Ω is the segmentation, so that the vector field propagates from the edges inwards to the medial axis.

The minimization of the energy functional can be obtained iteratively using an explicit time discretization parameter t and evolving the vector field as described in [6]. We furthermore normalize the vector field so the magnitude of the GVF is unity everywhere.

Medial Function: After solving the GVF optimization problem, the resulting vector field $\mathbf{v}(\mathbf{x})$ is smooth due to the diffusion term in the GVF energy. Therefore, spatial derivatives of the field can be computed and the divergence operator can be computed via:

$$\operatorname{div}\mathbf{V}(\mathbf{x}) = \frac{\partial u(\mathbf{x})}{\partial x} + \frac{\partial v(\mathbf{x})}{\partial y} + \frac{\partial w(\mathbf{x})}{\partial z}. \tag{5}$$

It describes the local expansion or contraction of the vector field.

Since the GVF vectors converge towards the medial curve, these regions exhibit negative divergence. Therefore, we compute an initial medial response $\forall \mathbf{x} \in \Omega$ using

$$\tilde{m}(\mathbf{x}) = \begin{cases} -\operatorname{div}\left(\mathbf{V}(\mathbf{x})\right), & \text{if } \operatorname{div}\left(\mathbf{V}(\mathbf{x})\right) < 0, \\ 0, & \text{otherwise.} \end{cases} \tag{6}$$

and then min-max normalize the response over Ω giving us the medial function $m(x)$. The magnitude of the medial function is determined by the local convergence of the GVF field. At the center of a tubular structure, vectors from opposite sides of the boundary are directed towards the same location, producing a local contraction of the field. Using (6) in (3) we find the solution of T.

Backtracking: Given the travel-time field $T(\mathbf{x})$ obtained by solving (2) with the source placed at the root $\mathbf{x}_r$, so that $T(\mathbf{x}_r) = 0$, the medial axis to an endpoint $\mathbf{e}_i$ is recovered by gradient descent on T. Because the minimal-cost path coincides with the steepest-descent curve of the arrival time, the centerline is the solution of the ordinary differential equation

$$\frac{d\gamma(s)}{ds} = \mathbf{f}\big(\gamma(s)\big), \qquad \mathbf{f}(\mathbf{x}) = -\frac{\nabla T(\mathbf{x})}{\|\nabla T(\mathbf{x})\|}, \qquad \gamma(0) = \mathbf{e}_i, \tag{7}$$

integrated until γ reaches $\mathbf{x}_r$. Numerically, (7) is solved with a second-order Runge-Kutta scheme similar to [6]. The iteration terminates once $\|\gamma - \mathbf{x}_r\| \leq 1$. Integration is constrained to remain within Ω and falls back to the grid if needed.

Root and Endpoint Detection: The root $\mathbf{x}_r$ is taken to be the centroid of Ω in the 10th axial slice that intersects the segmentation, which yields a stable seed inside the trachea.

The n endpoints $\{\mathbf{e}_i\}_{i=1}^{n}$ are not known a priori. We discover them jointly with their centerlines through an iterative procedure that repeatedly extracts the deepest remaining branch. We first compute the Euclidean distance transform D. We solve the eikonal equation (2) a second time with D substituted for m in the cost (3), producing the arrival-time field T_D.

The cost T_D provides a robust, monotone measure of geodesic depth from $\mathbf{x}_r$ whose largest value lies at the end of the longest centered path and thus marks the most distal tip. The cost T, built from the medial function m, supplies the well-centered gradient used for backtracking.

Starting from an empty visited set $\mathcal{O} = \emptyset$, we iterate the following steps as long as a reachable, unclaimed voxel remains $\{\mathbf{x} \in \Omega \setminus \mathcal{O} : T(\mathbf{x}) < \infty\} \neq \emptyset$.

1. we choose the deepest unclaimed voxel as $\mathbf{e} = \arg\max_{\mathbf{x} \in \Omega \setminus \mathcal{O}} T_D(\mathbf{x})$.
2. we trace back from $\mathbf{e}$ to $\mathbf{x}_r$ according to (7).
3. then we extend $\mathcal{O}$

$$\mathcal{O} \leftarrow \mathcal{O} \cup \bigcup_{\mathbf{x} \in \mathcal{C}_{\mathbf{e} \to \mathbf{x}_r}} B\big(\mathbf{x},\, D(\mathbf{x}) + \sigma(\mathbf{x})\big), \tag{8}$$

where $B(\mathbf{x}, r) = \{\mathbf{y} \in \Omega : \|\Phi(\mathbf{y}) - \Phi(\mathbf{x})\| \leq r\}$ is a ball with radius r and point $\mathbf{x}$ with $\Phi(i, j, k) = (i\Delta x, j\Delta y, k\Delta y)$ mapping voxel indices to physical coordinates, so the dilation radius respects anisotropic spacing. The margin σ decreases linearly along the branch from $\sigma_{\max}$ at the root $\gamma(0)$ to $\sigma_{\min}$ at the tip $\gamma(L)$, with $\sigma(s) = \sigma_{\max} - \frac{s}{L}(\sigma_{\max} - \sigma_{\min})$. Every extracted path runs to $\mathbf{x}_r$ and hence shares its proximal portion with branches found earlier. The margin σ prevents off-center voxels from being re-selected as spurious endpoints. Figure 2 displays the algorithm on an example airway.

Fig. 2. This plots highlights $\mathcal{O}$ over time. From the first three to the last iteration.

3.2 Branch Point Detection

From Section 3.1 we retrieve n centerlines $\{\mathcal{C}_i\}_{i=1}^{n}$, each a discrete line from the root $\mathbf{x}_r$ to a distinct tip. We then compute branching points by walking the paths outward from the root and detecting where they split.

More specifically, at each step we partition the current vertices $\{\mathcal{C}_i[k]\}$ by single-linkage clustering in physical space, treating two vertices as connected when $\|\Phi(\mathcal{C}_i[k]) - \Phi(\mathcal{C}_j[k])\| < \tau$. As long as the vertices form a single cluster, the paths still coincide, so we average them into a centroid that marks our final centerline. When the vertices fall into two or more clusters, a bifurcation is detected and we repeat the process from the new branches. The resulting tree carries averaged centroids as centerline points, their branching points and a generation label per branch, making the hierarchical topology of the airway tree explicit.

4 Results

We parameterize the GVF $\mu = 0.15$, $\Delta t = 0.5$ and optimize for 500 steps. In cases of higher resolution scans we lower Δt and increase the number of steps by factor

of change. We set $\alpha = \ln(1e6)$ to enforce "medialness" and for backtracking we use $h = 0.5$. For the path masking we choose $\sigma_{\max} = \max D(\mathbf{x})$ and $\sigma_{\min} = 5$. Lastly, we set $\tau = 2$ as the radius for branch point detection. The runtime per scan for each scan was 6.63s for our method vs. 21.41s for the baseline per scan on average over all 326 scans.

We evaluate our method against classical 3D thinning [8] and the airway tree parser provided by [24] to extract the branch information. The tree parser uses ad-hoc rules to correct errors produced by the skeleton and neighborhood connectivity to detect branching points. Both methods are applied to the same ground truth segmentations from publicly available datasets ATM22 [23] and AeroPath [17]. ATM22 provides 299, while AeroPath adds 27 manually annotated CTs. We provide only a qualitative evaluation of our method due to the absence of ground truth centerlines.

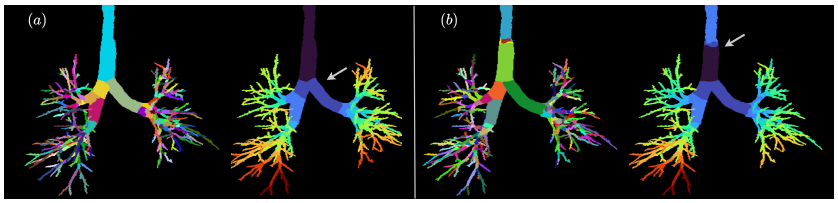

Fig. 3. Each plot presents a projection along the y axis onto the coronal plane. We display each voxel in the segmentation mapped to their closest branch and the evolution of generations. Here (a) shows our method, while (b) is achieved by thinning [8] and parsing [24].

Figure 3 contrasts the extracted branches of the two methods on a single airway. Noise in the segmentation causes the thinning algorithm to produce skeleton errors that the subsequent parsing could not recover, whereas our method extracts a clean skeleton that follows the topology of the airway.

We observe the same behavior across various cases with varying topology and airway size in Figure 4. In a few instances, e.g., case two, the post-processing manages to recover the correct branch from a faulty skeleton, but more commonly, the thinning errors propagate into the branch detection and corrupt the recovered hierarchy. We argue that this reflects a fundamental limitation of having to refine thinning-based approaches. Such corrections operate on a skeleton with already incorrect topological information. Our method sidesteps this problem by recovering the branch hierarchy directly from the centerlines and no repair stage is required.

The margin $\sigma_{\max}$ must be large enough to exclude every voxel along a traced path from endpoint detection, since an unmasked voxel could otherwise be selected as a spurious endpoint. This condition is easily met, but an overly large σ introduces the opposite risk of masking peripheral airways, leaving it untraced. We accept this trade-off and regard the loss of small airways as the the preferred

error mode, as it renders the recovered topology locally incomplete rather than incorrect.

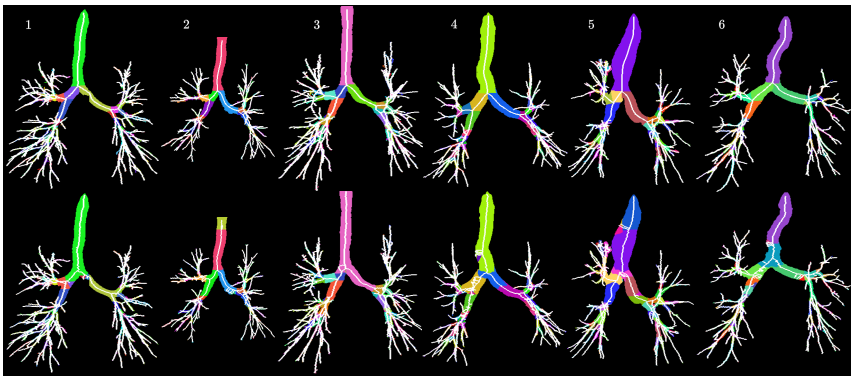

Fig. 4. Each column again displays a projection along the y axis. Each row shows the extracted centerline and each voxel mapped to their closest branch. The upper row shows our method and the bottom row the baseline. (1)-(3) show samples from ATM22 [23] while (4)-(6) show airways from Aeropath [17]

5 Discussion

The proposed method recasts centerline extraction as a set of minimum-cost paths through a centeredness field. Centerlines are obtained at subvoxel resolution and follow the continuous descent of the arrival time, so they are smooth rather than constrained to the voxel grid. The skeleton is thus not reconstructed from the voxel mask but revealed as the geometry of a field defined on it.

Every path shares a common root, branches coincide along their proximal course and separate only at bifurcations, so the branch and generation structure follows from the paths themselves rather than from a post-hoc parsing step. This convergence at bifurcations is induced by the medial function as the divergence of the GVF forms a sink wherever the inward flow from adjoining branches meets, ensuring that branches that share an anatomical course coincide in the extracted skeleton. The use of physical units throughout makes the extraction robust to anisotropic voxel spacing.

An implementation is publicly available at https://github.com/maltesilber/AirwayParser as a ready-to-use tool.

Acknowledgments. Funded by the European Union (ARTILLERY, No 101080983). Views expressed are those of the authors only; neither the European Union nor the granting authority can be held responsible for them.

Disclosure of Interests. The authors have no competing interests to declare that are relevant to the content of this article.

References

1. Adalsteinsson, D., Sethian, J.A.: A fast level set method for propagating interfaces. Journal of Computational Physics **118**(2), 269–277 (1995). https://doi.org/https://doi.org/10.1006/jcph.1995.1098, https://www.sciencedirect.com/science/article/pii/S0021999185710984
2. Burrowes, K., Doel, T., Kim, M., Vargas, C., Roca, J., Grau, V., Kay, D.: A combined image-modelling approach assessing the impact of hyperinflation due to emphysema on regional ventilation–perfusion matching. Computer Methods in Biomechanics and Biomedical Engineering: Imaging & Visualization **5**(2), 110–126 (2017). https://doi.org/10.1080/21681163.2015.1023358, https://doi.org/10.1080/21681163.2015.1023358
3. Cheung, W.K., Pakzad, A., Mogulkoc, N., Needleman, S., Rangelov, B., Gudmundsson, E., Zhao, A., Abbas, M., McLaverty, D., Asimakopoulos, D., Chapman, R., Savas, R., Janes, S.M., Hu, Y., Alexander, D.C., Hurst, J.R., Jacob, J.: Automated airway quantification associates with mortality in idiopathic pulmonary fibrosis. Eur Radiol **33**(11), 8228–8238 (Jul 2023)
4. Deschamps, T., Cohen, L.D.: Fast extraction of minimal paths in 3d images and applications to virtual endoscopy. Medical image analysis **5 4**, 281–99 (2001), https://api.semanticscholar.org/CorpusID:7292079
5. Dudurych, I., Pelgrim, G.J., Sidorenkov, G., Garcia-Uceda, A., Petersen, J., Slebos, D.J., de Bock, G.H., van den Berge, M., de Bruijne, M., Vliegenthart, R.: Low-dose CT-derived bronchial parameters in individuals with healthy lungs. Radiology **311**, e232677 (Jun 2024). https://doi.org/10.1148/radiol.232677
6. Hassouna, M.S., Farag, A.A.: Variational curve skeletons using gradient vector flow. IEEE Transactions on Pattern Analysis and Machine Intelligence **31**(12), 2257–2274 (2009). https://doi.org/10.1109/TPAMI.2008.271
7. Hassouna, M., Farag, A.: Robust centerline extraction framework using level sets. In: 2005 IEEE Computer Society Conference on Computer Vision and Pattern Recognition (CVPR'05). vol. 1, pp. 458–465 vol. 1 (2005). https://doi.org/10.1109/CVPR.2005.306
8. Lee, T., Kashyap, R., Chu, C.: Building skeleton models via 3-d medial surface axis thinning algorithms. CVGIP: Graphical Models and Image Processing **56**(6), 462–478 (1994). https://doi.org/https://doi.org/10.1006/cgip.1994.1042, https://www.sciencedirect.com/science/article/pii/S104996528471042X
9. Lo, P., van Ginneken, B., Reinhardt, J., Y., T., de Jong, P., Irving, B., Fetita, C., Ortner, M., Pinho, R., Sijbers, J., Feuerstein, M., Fabijanska, A., Bauer, C., Beichel, R., Mendoza, C.S., Wiemker, R., Lee, J., Reeves, A.P., Born, S., Weinheimer, O., van Rikxoort, E.M., Tschirren, J., Mori, K., Odry, B., Naidich, D., Hartmann, I., Hoffman, E., Prokop, M., Pedersen, J., de Bruijne, M.: Extraction of airways from CT (EXACT'09). IEEE Transactions on Medical Imaging **31**(11), 2093–2107 (Nov 2012). https://doi.org/10.1109/TMI.2012.2209674, http://dx.doi.org/10.1109/TMI.2012.2209674
10. Lo, P., Sporring, J., Ashraf, H., Pedersen, J.J., de Bruijne, M.: Vessel-guided airway tree segmentation: A voxel classification approach. Medical image analysis **14**(4), 527–538 (2010)
11. Nakano, Y., Muro, S., Sakai, H., Hirai, T., Chin, K., Tsukino, M., Nishimura, K., Itoh, H., Paré, P.D., Hogg, J.C., Mishima, M.: Computed tomographic measurements of airway dimensions and emphysema in smokers. correlation with lung function. Am. J. Respir. Crit. Care Med. **162**(3 Pt 1), 1102–1108 (Sep 2000)

12. Pakzad, A., Cheung, W., Moorsel, C.V., Quan, K., Mogulkoc, N., Bartholmai, B., Es, H.V., Ezircan, A., Beek, F.V., Veltkamp, M., Karwoski, R., Peikert, T., Clay, R., Foley, F., Braun, C., Savas, R., Sudre, C., Doel, T., Alexander, D., Wijeratne, P., Hawkes, D., Hu, Y., Hurst, J., Jacob, J.: Evaluation of automated airway morphological quantification for assessing fibrosing lung disease. Computer Methods in Biomechanics and Biomedical Engineering: Imaging & Visualization **12**(1), 2325361 (2024). https://doi.org/10.1080/21681163.2024.2325361, https://doi.org/10.1080/21681163.2024.2325361
13. Palágyi, K., Tschirren, J., Hoffman, E.A., Sonka, M.: Quantitative analysis of pulmonary airway tree structures. Comput Biol Med **36**(9), 974–996 (Aug 2005)
14. Quan, K., Shipley, R.J., Tanno, R., McPhillips, G., Vavourakis, V., Edwards, D., Jacob, J., Hurst, J.R., Hawkes, D.J.: Tapering analysis of airways with bronchiectasis. In: Angelini, E.D., Landman, B.A. (eds.) Medical Imaging 2018: Image Processing. vol. 10574, p. 105742G. International Society for Optics and Photonics, SPIE (2018). https://doi.org/10.1117/12.2292306, https://doi.org/10.1117/12.2292306
15. Ronneberger, O., Fischer, P., Brox, T.: U-net: Convolutional networks for biomedical image segmentation. In: Navab, N., Hornegger, J., Wells, W.M., Frangi, A.F. (eds.) Medical Image Computing and Computer-Assisted Intervention – MICCAI 2015. pp. 234–241. Springer International Publishing, Cham (2015)
16. Sato, M., Bitter, I., Bender, M., Kaufman, A., Nakajima, M.: Teasar: tree-structure extraction algorithm for accurate and robust skeletons. In: Proceedings the Eighth Pacific Conference on Computer Graphics and Applications. pp. 281–449 (2000). https://doi.org/10.1109/PCCGA.2000.883951
17. Støverud, K.H., Bouget, D., Pedersen, A., Leira, H.O., Amundsen, T., Langø, T., Hofstad, E.F.: Aeropath: An airway segmentation benchmark dataset with challenging pathology and baseline method. PLOS ONE **19**(10), 1–18 (10 2024). https://doi.org/10.1371/journal.pone.0311416, https://doi.org/10.1371/journal.pone.0311416
18. Tagliasacchi, A., Delame, T., Spagnuolo, M., Amenta, N., Telea, A.C.: 3D Skeletons: A State-of-the-Art Report. Computer Graphics Forum **35**(2), 573–597 (May 2016). https://doi.org/10.1111/cgf.12865, https://hal.science/hal-01300281
19. Tschirren, J., Hoffman, E.A., McLennan, G., Sonka, M.: Intrathoracic airway trees: segmentation and airway morphology analysis from low-dose ct scans. IEEE transactions on medical imaging **24**(12), 1529–1539 (2005)
20. van der Walt, S., Schönberger, J.L., Nunez-Iglesias, J., Boulogne, F., Warner, J.D., Yager, N., Gouillart, E., Yu, T., the scikit-image contributors: scikit-image: image processing in Python. PeerJ **2**, e453 (6 2014). https://doi.org/10.7717/peerj.453, https://doi.org/10.7717/peerj.453
21. Xu, C., Prince, J.: Gradient vector flow: a new external force for snakes. In: Proceedings of IEEE Computer Society Conference on Computer Vision and Pattern Recognition. pp. 66–71 (1997). https://doi.org/10.1109/CVPR.1997.609299
22. Zhang, M., Li, C., Xie, F., Liu, Y., Zhang, H., Wu, J., Zhang, C., Yang, J., Sun, J., Yang, G.Z., Gu, Y.: Airmorph: Topology-preserving deep learning for pulmonary airway analysis (2025), https://arxiv.org/abs/2412.11039
23. Zhang, M., Wu, Y., Zhang, H., Qin, Y., Zheng, H., Tang, W., Arnold, C., Pei, C., Yu, P., Nan, Y., et al.: Multi-site, multi-domain airway tree modeling. Medical Image Analysis **90**, 102957 (2023)
24. Zheng, H., Qin, Y., Gu, Y., Xie, F., Yang, J., Sun, J., Yang, G.Z.: Alleviating Class-Wise gradient imbalance for pulmonary airway segmentation. IEEE Trans Med Imaging **40**(9), 2452–2462 (Aug 2021)